

The impact of spiro-OMeTAD photodoping on the reversible light-induced transients of perovskite solar cells



Boer Tan, Dr. ^{a,b}, Sonia R. Raga, Dr. ^{a,b,c,*}, Kevin James Rietwyk, Dr. ^{a,b}, Jianfeng Lu, Dr. ^{a,b,d}, Sebastian O. Fürer, Dr. ^{a,b}, James C. Griffith ^e, Yi-Bing Cheng, Dr. ^{f,g}, Udo Bach, Dr. ^{a,b,h,i,**}

^a Department of Chemical Engineering, Monash University, Clayton, Victoria 3800 Australia

^b ARC Centre of Excellence in Exciton Science, Monash University, Clayton, Victoria 3800 Australia

^c Institut Català de Nanociència i Nanotecnologia, Universitat Autònoma de Barcelona, 08193 Bellaterra, Barcelona, Spain

^d State Key Laboratory of Silicate Materials for Architectures, Wuhan University of Technology 430070 Wuhan, China

^e Monash X-ray Platform, Monash University, Clayton, Victoria 3800 Australia

^f Department of Materials Science and Engineering, Monash University, Clayton, Victoria 3800, Australia

^g State Key Laboratory of Advanced Technology for Materials Synthesis and Processing, Wuhan University of Technology, Wuhan 430070 PR China

^h CSIRO Manufacturing, Clayton, Victoria 3168 Australia

ⁱ Melbourne Centre for Nanofabrication, Australian National Fabrication Facility, Clayton, Victoria 3168, Australia

ARTICLE INFO

Keywords:

Spiro-OMeTAD
Impedance spectroscopy
Photodoping
Hole injection barrier
Light Soaking

ABSTRACT

Hole transporting materials (HTMs) play essential roles in facilitating hole extraction and suppressing recombination in lead halide perovskite solar cells (PSCs). High levels of *p*-doping in HTMs is necessary for achieving high device performance, attributed to an increased electrical conductivity. In this work, we provide evidences that the poor performance of PSCs with low levels of doping (*i.e.*, 4 mol% spiro-OMeTAD⁺) in spiro-OMeTAD is mainly caused by the presence of a Schottky barrier at the perovskite/spiro-OMeTAD interface, hampering hole injection. Under continuous illumination at open-circuit condition, the barrier gradually diminishes, increasing the PSC power conversion efficiency by 70-fold after 7 h. This process is completely reversible, returning to the initial poor performance after dark storage. We attribute this improvement in performance to a gradual photodoping of spiro-OMeTAD, triggered by the transfer of photogenerated holes and mediated by the slow migration of halide anions from perovskite to compensate the newly formed spiro-OMeTAD⁺. In-situ parallel analyses with impedance spectroscopy (IS) and photoluminescence are employed to gain insights into the charge dynamics along with light soaking. We find that the Schottky barrier resistance overlays with the recombination signal at the high frequency arc of IS, having important implications for the IS data analysis for PSCs. The work elucidates a major mechanism causing the slow efficiency variations during light/dark cycling, commonly observed in PSCs, which complicates the determination of long-term stability.

1. Introduction

Despite the certified excellent power conversion efficiency (PCE) exceeding 25% [1], PSCs still suffer from a variety of transient behaviors that interfere with its characterisation. In particular, the slow transients that take place in the range of minutes to hours complicate the analysis of the stable operation in the long term, which is a key milestone for the development of this type of photovoltaic technology [2]. When

measuring the PCE under dark-illumination cycles, the response of the PSC varies among publications [3]. In the literature, there are several reports on devices experiencing both gain and loss during light soaking and some of the performance is reversible when being stored in the dark [4–8]. Moreover, a single device can exhibit both behaviors when the performance is being tracked for a long time, suggesting that multiple processes are behind the light soaking observations [2]. Previous works have studied the physical origins of these slow transient behaviors by

* Corresponding author at: Institut Català de Nanociència i Nanotecnologia, Universitat Autònoma de Barcelona, 08193 Bellaterra, Barcelona, Spain.

** Corresponding author at: Department of Chemical Engineering, Monash University, Clayton, Victoria 3800 Australia.

E-mail addresses: Boer.Tan@monash.edu (B. Tan), Sonia.Ruizraga@icn2.cat (S.R. Raga), Kevin.Rietwyk@monash.edu (K.J. Rietwyk), Jianfeng.Lu@whut.edu.cn (J. Lu), Sebastian.Furer@monash.edu (S.O. Fürer), James.Griffith@monash.edu (J.C. Griffith), Yibing.Cheng@monash.edu (Y.-B. Cheng), Udo.Bach@monash.edu (U. Bach).

analysing perovskite ion migration/accumulation at the interfaces or photoinduced trap filling [6,9,10]. Most of these works focused on electron transporting materials (ETMs) such as TiO_2 and SnO_2 . For instance, TiO_2 was reported to form weak Pb-I-Ti bonds [9], creating light-induced oxygen vacancies [11], or inducing UV-promoted trap formation [6], among others [12–14]. The role of the interactions between organic HTMs and the perovskite layers has been generally overlooked when analysing the causes of slow reversible transients and/or degradation mechanisms in PSCs. Being the most broadly employed HTM, 2,2',7,7'-tetrakis(*N,N*-di-*p*-methoxyphenyl-amine)-9,9'-spirobifluorene (spiro-OMeTAD) has consistently demonstrated high device performance but still suffers from the following limitations: (i) it needs additives and arbitrary air-exposure times to achieve adequate conductivity [15], (ii) the additives can segregate within the spiro-OMeTAD layers or cause internal reactions that change the electrical properties and morphology of spiro-OMeTAD [16–18], (iii) small cations from the additives can diffuse through the perovskite layer and alter the device performance and hysteresis [19], (iv) illumination and heat affects the oxidation levels of spiro-OMeTAD, modifying its conductivity [20–22] and (v) the oxidised species spiro-OMeTAD⁺ can promote chemical reactions with the halide anions in the perovskite [9]. Overall, spiro-OMeTAD is a selective contact that can indeed play a significant role, by itself or in conjunction with other processes, in defining the transient and long-term operation of PSCs; yet the implications are largely unknown.

The scope of this work is to provide a comprehensive study on how the properties of the spiro-OMeTAD layer affects the slow but dramatic gain in PCEs under illumination [23]. For that, we have carefully modified the spiro-OMeTAD conductivity by tuning the amount of pre-oxidised spiro-OMeTAD²⁺ in the absence of metal additives/dopants such as Li^+ , $\text{Cu}^{1+/2+}$ or $\text{Co}^{2+/3+}$ complexes without air exposure. We have observed extremely poor PCEs for PSCs with a spiro-OMeTAD layer that has low electrical conductivity. With detailed characterisation using IS, photoluminescence (PL) and the support from electrical modelling of the J-V curves. We demonstrate that the weak performance is not only caused by a significant series resistance but also by the presence of a Schottky barrier at the perovskite/spiro-OMeTAD interface. During light soaking, the series resistance and hole injection barrier are gradually reduced. Surprisingly, the recombination mechanisms are not obviously affected during most of the light soaking period and such conclusions cannot be drawn just from IS interpretation. Finally, we propose a reversible photodoping mechanism for the spiro-OMeTAD layer in which the migration of halide anions in the perovskite layer promotes the oxidation of spiro-OMeTAD and the reduction of spiro-OMeTAD⁺ under illumination and dark conditions, respectively. We expect that this study will provide insights for a better selection of HTMs with optimum electrical and electronic properties by maintaining the long-term stability of the HTM conductivity in PSCs. The analyses in this work provide essential information to assess one of the multiple causes for the degradation and light soaking transients observed in PSC stability studies.

2. Results and discussion

A device structure of FTO/c-TiO₂/mp-TiO₂/Rb_{0.05}Cs_{0.05}FA_{0.8}-MA_{0.07}PbBr_{0.4}I_{2.57}/HTM/Au (c-TiO₂-compact titania layer; mp-TiO₂-mesoporous titania layer; FTO- glass coated with fluorine-doped tin oxide) is used in this work. To study the effects of HTM properties on the performance of PSCs, we utilized two types of devices fabricated with either 2 mol% or 16 mol% of spiro-OMeTAD(TFSI)₂ in the HTM formulation. More fabrication details can be found in the [Supporting Information](#). The addition of spiro-OMeTAD(TFSI)₂ readily provides oxidised spiro-OMeTAD⁺ species in the spiro-OMeTAD films. As shown in our previous work, there is a linear relationship between the mole fraction of spiro-OMeTAD(TFSI)₂ and the HTM conductivity [24,25]. According to our previous study, 14 mol% of spiro-OMeTAD(TFSI)₂ is

sufficient to provide optimal PCEs for PSCs in the absence of air exposure or lithium salts, which are comparable to PSCs with HTMs fabricated with lithium salts in air [24].

Fig. 1a shows the current density-voltage (*J*-*V*) curve for the PSC with 16 mol% spiro-OMeTAD(TFSI)₂ which was referred to as devices with high content of spiro-OMeTAD⁺ and abbreviated as "HC". At the beginning of the experiments (*t* = 0) the HC device shows excellent photovoltaic properties with $J_{\text{SC}} = 23.1 \text{ mA}\cdot\text{cm}^{-2}$, $V_{\text{OC}} = 1.13 \text{ V}$, fill factor (FF) = 72% and a PCE of 18.9% scanning from forward bias (FB) to short circuit (SC). This is among the best PCEs reported for this device configuration in the absence of lithium bis(trifluoromethanesulfonyl) imide (LiTFSI) and air exposure. **Fig. 1b** shows a typical *J*-*V* curve of a device with 2 mol% of spiro-OMeTAD(TFSI)₂ which is referred as the PSC with low content of spiro-OMeTAD⁺ and abbreviated as "LC". At *t* = 0, the LC device has a negligible PCE of 0.2% but, when kept under illumination at open circuit conditions, the photovoltaic parameters gradually improve. The evolution of the parameters *versus* light soaking time is illustrated in **Fig. S1a** and will be described briefly as follows. Both the J_{SC} and V_{OC} show dramatic improvement from 1.5 to 21.3 $\text{mA}\cdot\text{cm}^{-2}$ and 0.91–1.08 V within the first 30 min and eventually reach 23.2 $\text{mA}\cdot\text{cm}^{-2}$ and 1.07 V (stabilised) after 7 h. In contrast, the FF and the subsequent PCE, show a steady and gradual increase over the 7 h period, rising from 17% to 60% and 0.2–14.2%, respectively. It is worthwhile to note that the FF values at initial stages of the light soaking are below 25% producing an "s-shape" in the *J*-*V* curves. Since a high series resistance and/or low shunt resistance will deliver a FF equals to 25%, the traditional diode equation including shunt and series resistance is not sufficient to explain this behavior. The "s-shape", often observed in organic solar cells [26,27], and PSCs fabricated with pristine spiro-OMeTAD [15,28–30], is usually attributed to a charge accumulation mechanism at the interfaces. To the best of our knowledge, this is the first report showing the elimination of the "s-shape" *via* light-soaking of the device, suggesting a complex interaction between the perovskite and the LC HTM, which will be explored in detail below.

At this point we would like to emphasise two interesting observations; firstly, the PCE improvement under light soaking is reversible, *i.e.* the device performance will revert to the initial *t* = 0 state after storage in the dark. Secondly, the performance recovery shown in **Fig. 1b** is hampered when the LC device is illuminated at short circuit conditions, see **Fig. S1b**. The FF remains fixed to values around 25% after the first 15 min of illumination, limiting the photocurrent despite a slight improvement in the V_{OC} . This observation also rules out irradiation heating effects on the performance recovery of the device.

To analyse this gradual improvement in the device performance, we carry out IS analysis, which is a frequency-resolved technique that allows one to decouple the physical processes occurring at different time scales. IS spectra were collected at various applied voltages (V_{app}) from 0.3 to 1.1 V for the LC devices at incremental stages of the light soaking, as well as for the HC devices. We note that the IS spectra of the HC device had negligible variations during light soaking, therefore only the measurement at *t* = 0 is shown. In general, three arcs can be observed in the Nyquist (Z' - Z'') plot, examples are shown in **Fig. 2a** for both HC and LC devices at *t* = 0 as well as LC device after different light soaking intervals, **Fig. 2b,c**. We label the arc features according to the range of frequencies they span, *i.e.* around 1–100 Hz is low frequency (*lf*), between $\sim 10^4$ – 10^5 Hz high frequency (*hf*) and over 10^5 Hz very high frequency (*vhf*). The peaks on the Bode (*phase-frequency*) plot, **Fig. 2d**, and the "plateaus" in the capacitance-frequency plot, **Fig. 2f**, provide a visual support to easily identify the characteristic frequencies where the arcs appear. The IS spectra were fitted to the equivalent circuit shown in **Fig. 2e**, composing of three *R/CPE* elements and a resistor in series. Constant phase elements (CPEs) were used to model the non-ideal capacitances [31]. The choice of such a simplified circuit is supported by the work of Todinova *et al.* which demonstrates that the values of the fitted parameters (*i.e.*, resistances, capacitances and time constants) are similar for most of the equivalent circuits found in the literature,

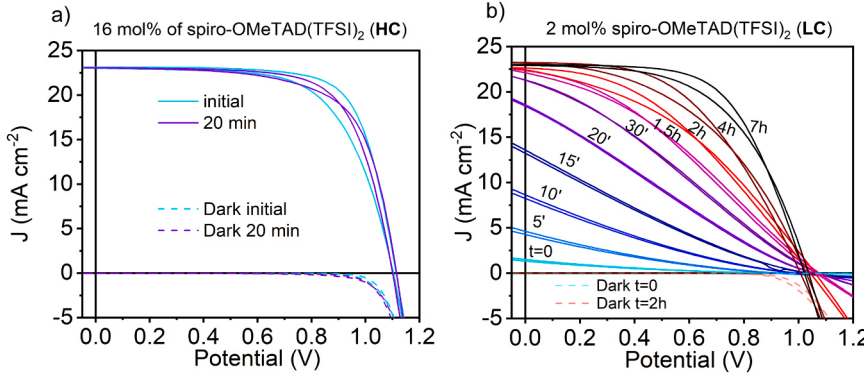


Fig. 1. Evolution of the J - V curves during light soaking for PSCs fabricated with a) 16 mol% spiro-OMeTAD(TFSI)₂ which is referred as PSC with high content of spiro-OMeTAD⁺ and abbreviated as “HC” and b) devices with 2 mol% spiro-OMeTAD(TFSI)₂ which is referred as PSC with low content of spiro-OMeTAD⁺ and abbreviated as “LC”. All J - V curves have been measured in both directions from forward bias (FB) to short circuit (SC) (1.2 to -0.1 V) and vice versa (-0.1 to 1.2 V) at a scan rate of 100 mV s^{-1} . A white LED illumination was adjusted to produce device photocurrent equivalent to which was measured under 1 sun and the devices were kept at open-circuit conditions during the light soaking as indicated in the legend between J - V scans.

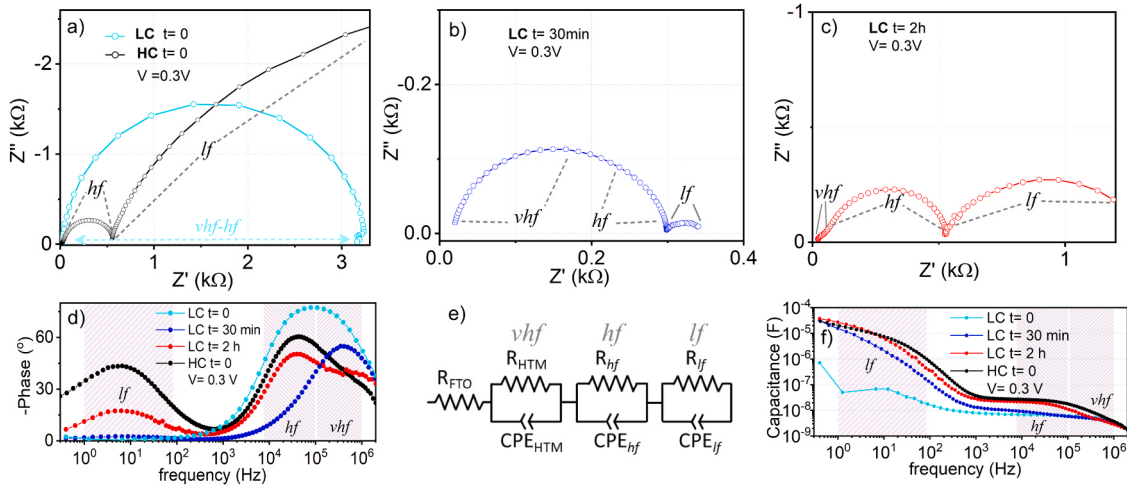


Fig. 2. The arc features in the IS of the HC device and LC device at different stages of the light soaking. Nyquist plots show different arc magnitudes at the same applied voltage, 0.3 V a) $t = 0$ for the LC and HC cell, and the LC cell at b) $t = 30\text{ min}$ and c) $t = 2\text{ h}$ of light soaking. d) Bode (phase-frequency) and f) capacitance-frequency plots are helpful to identify the different features. The low (lf), high (hf) and very high (vhf) frequency features are indicated as a guide in all plots and the circuit. e) Simplified equivalent AC circuit employed for the fitting of all IS data.

provided that inductive elements are not present [32].

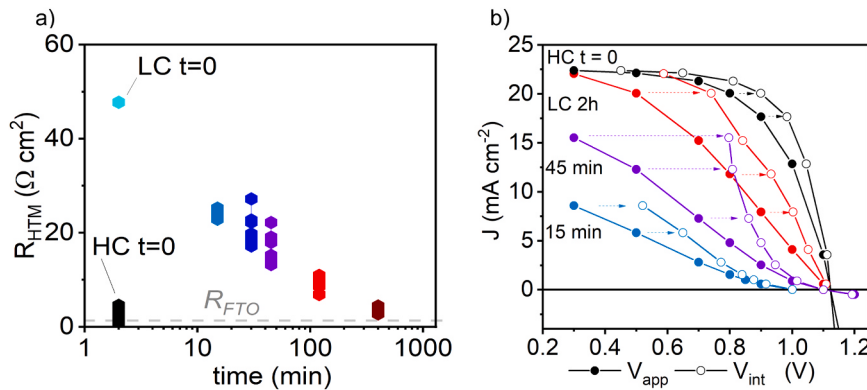
In Fig. 2f, from left to right, the first resistor R_{FTO} is a non-capacitive resistance caused mostly by the external contacts and FTO. The second circuit element at vhf is the average resistance of the HTM layer, and its associated capacitance CPE_{HTM} [24,30,33]. The interpretation of the features found at hf and lf varies among reports, we provide an overview as follows. For the best performing PSCs, at high voltages near V_{oc} , the sum of the resistances fitted from the features at hf and lf directly relates to the total recombination resistance (R_{rec}) and $R_{rec} = R_{hf} + R_{lf}$ [34–39], with a characteristic exponential voltage dependence expressed as:

$$R_{rec} = R_0 \exp\left(-\frac{qV_{int}}{n_{IS} k_B T}\right) \quad (1)$$

where R_0 is the recombination resistance at short circuit, q is the elementary charge, V_{int} is the voltage across the perovskite layer, n_{IS} is the ideality factor, T is the temperature and k_B is the Boltzmann constant. In this interpretation, CPE_{hf} in parallel with R_{rec} and is generally attributed to the geometric capacitance (C_g) of the perovskite layer, similar to a dielectric double-plate capacitor. Since the dielectric constant is a property of the perovskite material, C_g is not expected to change. However, the variations observed for CPE_{hf} in Fig. 2f suggest that it cannot be solely assigned to C_g .

The origin of the split in the recombination arcs into hf and lf signals, as well as the origin of the CPE_{lf} , is still under debate. However, an increasing consensus attributes it to the coupled effect of mobile ions in the perovskite. In this scenario, when applying the 10 mV voltage

perturbation, the “slow” ions are unable to follow the fast electrical field changes at hf , but they do respond to the lf perturbations partially screening the electric field thus causing the apparent lf capacitance [36, 38,40,41]. In contrast, other reports where devices with relatively lower efficiencies were measured, assigned the hf arc to (i) the electron transport resistance of the ETM [42,43], (ii) charge transport resistance of the perovskite layer [44,45], and (iii) injection processes at the perovskite/ETM interface [36,46]. Some of the controversy can be understood thanks to a recent work which for the first time demonstrates that the electron transport resistance and chemical capacitance of sufficiently thick mesoporous TiO₂ layers will overlay in the recombination IS arcs, adding up to the total resistance $R_{hf} + R_{lf}$ [47]. However, our observations are different from the previous reports, thus in Fig. 1e we have not assigned physical meanings to the hf and lf arcs. This is because, according to our findings below, there are two different processes behind the hf arc. The lf arc does not have a physical meaning by itself. For the sake of completeness, and to put into this context with the state-of-the-art literature, we advance the complete equivalent circuit in Fig. S2, deduced after our findings below. However, this circuit will not be used for further discussion in this manuscript, the reader may use it as a guide to understand the distribution of all physical processes within the PSCs. The J - V curves extracted from the IS scans from the DC current and DC voltage are plotted as solid circles in Fig. 3b. Note that these J - V curves represent the actual performance of the device simultaneous with the IS measurement. Despite the long time required to collect all IS data points (~ 2 min per point), the “light soaking” evolution of the LC device



is similar to the J - V curves obtained at 100 mVs^{-1} in Fig. 1b, ensuring the validity of the measurement. The times used in the J - V_{app} labels are indicative of the start of the voltage scan e.g. LC $t = 0$ is the first point. Fig. 3a shows the evolution of the HTM resistance (R_{HTM}) for the LC device at incremental light exposure times as well as the HC device at $t = 0$. The fitted values of R_{HTM} exhibit a small variation along the V_{app} , partially influenced from the intrinsic error while fitting the IS. The variation is shown in Fig. 3a as scattered points. However, it is clear that the overall R_{HTM} values decrease progressively with longer light exposure times. The HTM conductivity (σ_{HTM}) can be obtained through the following expression: $\sigma_{HTM} = d/(R_{HTM}A)$, where d is the HTM thickness and A is the active area. For the LC cell at $t = 0$, σ_{HTM} is around $4.2 \times 10^{-5} \text{ S cm}^{-1}$, which is close to the reported conductivity of pristine spiro-OMeTAD [25,30,48,49]. After 4 h illumination, the conductivity increases up to $6.0 \pm 1.1 \times 10^{-4} \text{ S cm}^{-1}$, whereas it is $1.2 \pm 0.8 \times 10^{-3} \text{ S cm}^{-1}$ for the HC cell and this is comparable to the conventional spiro-OMeTAD layer with lithium additives and air-exposure [48].

The photoinduced oxidation process of spiro-OMeTAD is known as “photodoping”. Some previous works suggest that the presence of oxygen molecules in the proposed oxidation reactions is compulsory [20, 50–52]. However, Sanchez *et al.* demonstrated that the light-induced oxidation of pristine spiro-OMeTAD in solution can take place under inert atmosphere and the speed of oxidation is accelerated by the presence of additives or bubbling air into the solution [52]. In addition, Wang *et al.* showed that the photodoping mechanism of spiro-OMeTAD in PSCs with air exposure is spectrum dependent and the oxidation of spiro-OMeTAD can be triggered under illumination at higher wavelengths (*i.e.* $> 450 \text{ nm}$) when the perovskite layer is present. Here we prepared encapsulated devices, which were not exposed to air at any stage during the fabrication or characterisation process. We therefore are able to rule out the presence of oxygen within the encapsulation gap. In addition, the *p*-dopant spiro-OMeTAD(TFSI_2) readily provides oxidised spiro-OMeTAD $^{+}$ species, whereas its counter-ion TFSI^- or the other additive 4-*tert*-butylpyridine (*t*-BP) is unlikely to participate in further light-induced oxidation reactions. On this basis, we suggest that the photogenerated holes in the perovskite layer are the main cause of the photodoping in our HTM system. Furthermore, the oxidised species could revert to neutral spiro-OMeTAD when the device is kept under dark, causing the reversibility in device performance explained above.

As R_{HTM} and R_{FTO} are located at the external layers of the sandwich device, a considerable voltage drop at V_{app} will occur across these layers affecting the internal voltage of the device (V_{int}). Considering the large variations in R_{HTM} for the LC device during light soaking, the voltage at the internal part of the solar cell, *i.e.* perovskite bulk and TiO_2 /perovskite/HTM interfaces see Fig. S4, will evolve accordingly. In order to allow for a fair comparison between measurements of R_{hf} and R_{lf} without considering the voltage drop caused by the series resistance, V_{int} was calculated as:

Fig. 3. a) Evolution of the R_{HTM} obtained by fitting the $v hf$ feature from IS (normalised to the active area) is plotted versus the light soaking time. The scattered points are the values at all the applied voltages where LC and HC at $t = 0$ are plotted at the time of 2 min for clarity. R_{FTO} is similar for all measurements and the average value (grey dash line) is shown in the plot as a guide. b) The DC current-applied voltage (J - V_{app} , solid circles) values extracted from the IS data for the LC device at various light soaking times ($t = 15 \text{ min}, 45 \text{ min}$ and 2 h) and the HC device at $t = 0$. Curves with open circles are plotted after correcting the voltage drop (represented as arrows) caused by $R_{FTO} + R_{HTM}$; *i.e.* current vs. the internal voltage (J - V_{int}).

$$V_{int} = V_{app} + J \cdot (R_{HTM} + R_{FTO}) \quad (2)$$

The J - V_{int} curves plotted in Fig. 3b shows how the different voltage drops depend on the current density and R_{HTM} with light soaking of the LC device.

For the HC device, (black symbols in Fig. 4) both R_{hf} and R_{lf} have a decreasing trend with V_{int} , especially approaching V_{oc} . The less pronounced voltage-dependence below the maximum power point ($V_{MPP} \sim 0.8 \text{ V}$) is an effect of the existing shunt resistances. Similar trends have been observed for high performance PSCs, where it has been proposed that the sum of R_{hf} and R_{lf} is equivalent to the recombination resistance of the device (R_{rec}) [34–39,53]. As R_{rec} is expected to follow the exponential relation shown in Eq. (1) at voltages between the V_{MPP} and V_{oc} , we can extract the device ideality factor n_{IS} (see Fig. 5a) to gain insights into the device recombination mechanisms [34–39,53]. For the HC device, R_{lf} provides an ideality factor of $n_{IS} = 1.5$, a value typical for Schottky-Read-Hall (SRH) recombination, and is commonly reported for PSCs [53,54]. However, higher ideality factor values, $2 < n_{IS} < 5$ for R_{hf} of the HC device and LC $t = 2$ and 4 h , cannot be easily attributed to any recombination mechanisms. In the literature, ideality factors greater than 2, obtained either by IS, transient methods or Suns- V_{oc} , have been attributed to device polarization, electrostatic effects of the mobile ions and multiple trapping recombination [54–56]. In order to understand whether these mechanisms are actually influencing the LC device, we further analysed the ideality factor using the Suns- V_{oc} method.

For that, we have measured the device V_{oc} at different light intensities (P_{light}) (Fig. S5) and calculated the differential ideality factor n_d through Eq. (3) [54].

$$n_d = \frac{q}{k_B T} \frac{\partial V_{oc}}{\partial \ln(P_{light})} \quad (3)$$

With the Suns- V_{oc} , the effects of parasitic resistances on the determination of n_d are eliminated [54,56]. In addition, despite the apparent linear relation of V_{oc} vs. $\ln(P_{light})$, see Fig. S5, by analysing the derivative instead of a linear regression we can account for the different slopes enabling a more accurate analysis [54,57]. Fig. 5b shows that, compared to n_{IS} , there is little variation in the values of n_d for the LC device between 25 min and up to 3.5 h of light soaking, which is also similar to the n_d of the HC device. The ideality factors n_d range from values close to 2 at lower light intensities to $n_d \approx 1$ at intensities close to 100 mWcm^{-2} , suggesting a change in the dominant recombination mechanisms from trap-mediated to band-to-band [54,55]. The average value is around $n_d \approx 1.5$, matching the ideality factor extracted from the J - I arc in IS for the HC device and equals to the typically reported ideality factors for high efficiency perovskite devices [53–56]. Moreover, for the LC device at $t = 10 \text{ min}$, n_d is less than 1, similar low values have been observed after “poling” the PSCs and were attributed to the activation of recombination sites after ionic accumulation at the interfaces [55]. In summary, ideality factors extracted from the Suns- V_{oc} for the LC device suggest that

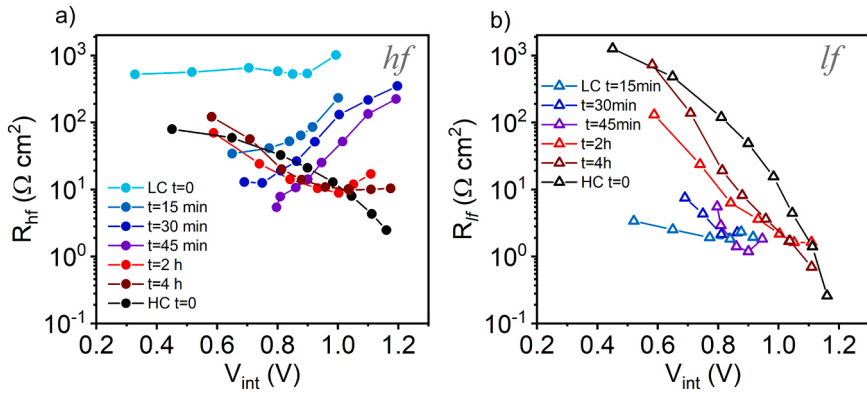


Fig. 4. a) High frequency resistance (R_{hf}) and b) low frequency resistance (R_{lf}) fitted from IS data plotted vs. the internal voltage V_{int} for the LC device from $t = 0\text{--}4\text{ h}$ light soaking times as well as the HC cell at $t = 0$.

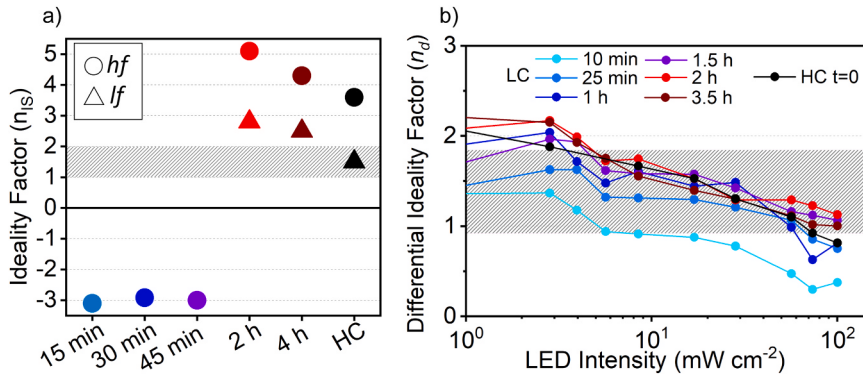


Fig. 5. a) Ideality factors (n_{IS}) of the LC device during light soaking from $t = 15\text{ min}$ to $t = 3.5\text{ h}$ and $t = 0$ for the HC device obtained by applying Eq. (1) to the R_{hf} (circles) and R_{lf} (triangles). b) Differential ideality factors (n_d) obtained by applying Eq. (3) to the Suns- V_{oc} measurement at different stages of light soaking. We therefore conclude that the large ideality factors n_{IS} extracted from R_{hf} and R_{lf} for the LC device at $t = 2\text{ h}$ and 4 h , see Fig. 5a, is an artifact created by the presence of an additional series resistance, in addition to the previously determined R_{HTM} and R_{FTO} [58]. Such series resistance causes an additional voltage drop that can be seen as a decreased slope in the recombination resistance for the LC device at $t = 2\text{ h}$ and 4 h in Fig. 4a-b, which is also observed in the J-V curves in Fig. 3a as the lower FF.

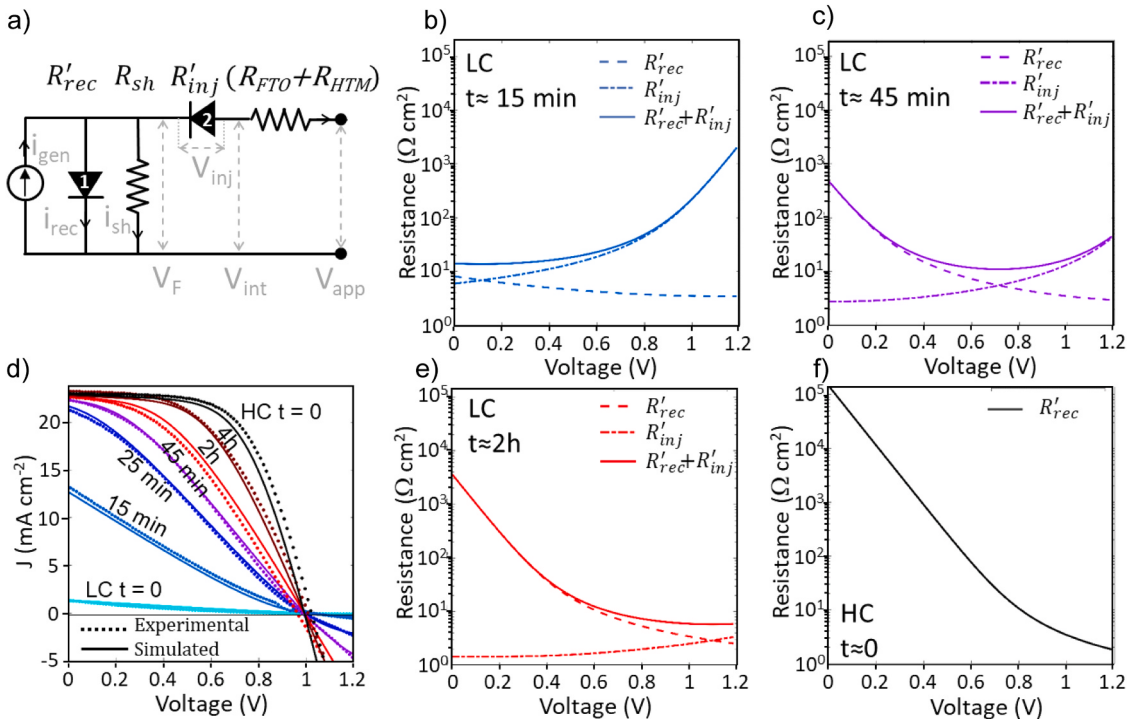


Fig. 6. a) Equivalent DC circuit used for the simulation of the ‘s-shape’ J-V curves shown in d) as solid lines, the dotted lines in d) are the experimentally obtained J-V curves for the LC device at different times of the light soaking and for the HC device at $t = 0$. b), c), e), f) Simulated R'_{rec} (long dash) and R'_{inj} (dash-dot) extracted from the simulated J-V curve parameters at different light soaking times as well as the sum $R'_{rec} + R'_{inj}$ (solid line) that simulates the $R_{hf} + R_{lf}$ obtained from IS shown in Fig. 4, for LC b,c,e) and HC f) devices where $R'_{inj} = 0$.

the recombination mechanisms may be altered by the hole accumulation only for the first 25 min of light soaking.

Recalling Fig. 4a for the LC device illuminated for $t = 15, 30$ and 45 min, R_{hf} increases exponentially with V_{int} which is reflected in Fig. 5a as negative ideality factors with surprisingly constant values around $n_{IS} = -3$. This is clear evidence that R_{hf} for the LC device at the beginning of the light soaking originates from a different physical process rather than charge recombination. We propose that R_{hf} is mainly contributed by a voltage-dependent hole injection resistance that we will refer to as R_{inj} in the following discussion. It appears that the presence of R_{inj} strongly correlates to the “s-shape” of the J-V curves shown in Fig. 1b and 3a. As introduced above, FF values below 25% cannot be modelled with the classical diode equation by just including an ohmic series resistance drop, therefore, a more complex scenario accounting for a voltage-dependent series resistance needs to be introduced. On this basis, we have simulated the J-V curves by simply adding a diode in series with the terminal, between R_{rec} and ($R_{FTO} + R_{HTM}$), as shown in Fig. 6a. This diode acts as a voltage-dependent series resistance and has been used by others to model a Schottky barrier at a selective contact. Similar approaches with different degrees of complexity have been previously reported to model the “s-shape” in J-V curves [59–62].

To understand the impact of the additional resistance, we will begin from discussing the current through the device using the typical equivalent circuit model before addressing the voltage losses caused by R_{inj} and the influence it plays on the other circuit elements.

$$I = I_{sc} - I_{01} \left(\exp\left(\frac{qV_F}{n_1 k_B T}\right) - 1 \right) - \frac{V_F}{R_{sh}} \quad (4)$$

where I_{sc} is the short circuit current of the device, I_{01} is the dark current across diode 1, n_1 is the ideality factor of diode 1 and V_F is the voltage across diode 1 (representing R_{rec}) and R_{sh} is the shunt resistance (see Fig. 6a). We employ the Shockley diode equation to model the voltage drop caused by R_{inj} :

$$V_{inj} = \frac{n_2 kT}{q} \ln\left(\frac{I + I_{02}}{I_{02}}\right) \quad (5)$$

where n_2 is the ideality factor and I_{02} is the dark current of diode 2. By using $V_F = V_{int} + V_{inj}$, we can substitute Eq. (5) into the traditional solar cell diode equation, Eq. (4). The equation used for simulating the “s-shape” of J-V curves takes the following form:

$$I = I_{sc} - I_{01} \left(\exp\left(\frac{qV_{int}}{n_1 k_B T}\right) \exp\left(\frac{n_2}{n_1} \ln\left(\frac{I + I_{02}}{I_{02}}\right)\right) - 1 \right) - \frac{V_F}{R_{sh}} \quad (6)$$

The J-V curves were simulated by numerically solving Eq. (6) and plotted as solid lines in Fig. 6d which agrees well with the original data (dotted lines). In order to further reduce the number of parameters, we have set the ideality factors to $n_2 = n_1 = 3$ based on the ideality factors obtained for R_{inj} in Fig. 5a and an approximation of n_{IS} obtained for $R_{hf} + R_{lf}$ of the HC device (see Fig. 5). We also set $R_S = R_{FTO}$ at $V = 0.8$ V and used I_{02} as a fitting parameter to scale R_{HTM} ; the rest of the parameters were determined from cursory fits of the data and fixed for the simulations. Further details on the simulation and the list of parameters can be found in the Supporting Information.

Furthermore, the simulated recombination and hole injection resistances R'_{rec} and R'_{inj} can be calculated from the expressions of diodes 1 and 2, respectively, as:

$$R'_{rec} = \frac{dV_{int}}{dl_{rec}} \quad (7)$$

$$R'_{inj} = \frac{dV_{inj}}{dI} \quad (8)$$

The simulated R'_{rec} and R'_{inj} are plotted in Fig. 6b,c,e,f during light soaking at $t = 15$ min, 45 min and 2 h for the LC device, and the HC

device at $t = 0$. We emphasise that the sum of $R'_{rec} + R'_{inj}$ closely reflects the $R_{hf} + R_{lf}$ measured from IS shown in Fig. 4. At initial stages of the light soaking, i.e. $t = 15$ min, R'_{inj} is significantly larger (dash-dot line in Fig. 6b) and is the dominating resistance across the V_{app} range. With increasing time of light soaking, see Fig. 6c, R'_{inj} is reduced but remains significant at voltages close to V_{oc} and causes a plateau in the combined resistance (solid line) after 2 h as shown in Fig. 6e. This trend can be observed in Fig. 4 and provides a clear physical explanation for both the IS and J-V results. When R_{inj} is negligible, the main resistance governing the J-V curve is R_{rec} , which is seen in Fig. 6f (black solid line) and Fig. 4 (black symbols).

In order to gain further understanding of the origins of the injection resistance, we have characterised the PL response of the perovskite in a LC device at different times of light soaking as shown in Fig. 7b. We performed concurrent J-V measurements (Fig. 7a) to confirm that the device behaved similarly to the J-V performance in Fig. 1b, which is clearly the case given the presence and subsequent reduction in the “s-shape” with light soaking. For the PL measurements, a band pass filter was used to capture the peak PL from the perovskite film with minimal contribution from other layers, i.e. FTO, TiO_2 or HTM. For a high efficiency solar cell, the PL intensity should be minimal close to short circuit conditions due to the efficient extraction of photogenerated carriers and increase exponentially approaching open circuit conditions, where no carriers are extracted and therefore are forced to recombine. However, the high PL intensity at $t = 0$ indicates that there is a relatively high level of radiative recombination within the perovskite film independent of V_{app} . During light soaking, the PL gradually decreases at all V_{app} but the decrease is more pronounced at low bias voltage close to 0 V by over 1.5 orders. At $t = 4$ h the PL increases exponentially from J_{sc} to V_{oc} as expected for a good performing device. This evolution during light soaking can be understood considering that the changes in the PL reflect changes in V_F . At $t = 0$ V_F is closer to open circuit conditions independent of V_{app} , caused by a large voltage drop at the series resistances identified above R_{inj}, R_{FTO} and R_{HTM} . A reduction in PL corresponds to a likewise drop in the series resistances.

Through comprehensive analysis of the IS spectra and PL measurements, we have unraveled the presence of a hole injection barrier at the perovskite/HTM interface for devices with initially low content of spiro-OMeTAD⁺ in the HTM. We show that light soaking under open circuit conditions improves the conductivity of the HTM in the device, as well as gradually diminishing the hole injection barrier. However, under short circuit conditions (see Fig. S1b), light soaking only has an impact on the first 15 min and, with longer illumination times, the “s-shape” of the J-V curve remains. In the following, we will suggest and discuss the mechanisms that give rise to these observations by first addressing the changes in the HTM conductivity and then creating a link to the interfacial barrier.

Initially, the conductivity of the HTM (without LiTFSI or air exposure) increases during light soaking in the encapsulated PSC as shown in Fig. 3b. On the basis of similar previous observations for spiro-OMeTAD photodoping [51,52], the photogenerated holes (h^+) from perovskite will promote the oxidation reaction for neutral spiro-OMeTAD and lead to the formation of spiro-OMeTAD⁺. The charge neutrality is maintained due to the presence of negative charges. In contrast with previous reports [51,52], the HTM used in our work does not contain additional TFSI⁻ counter ions that are from LiTFSI and has not been exposed to air. We propose that the counter-balancing charges are provided by the available mobile anions from the perovskite lattice, i.e. I^- or Br^- , Fig. 8a, b. The proposed mechanism for these reactions is:



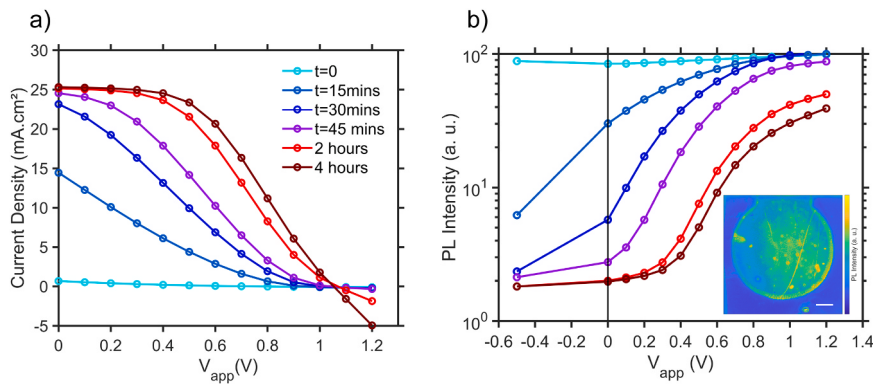
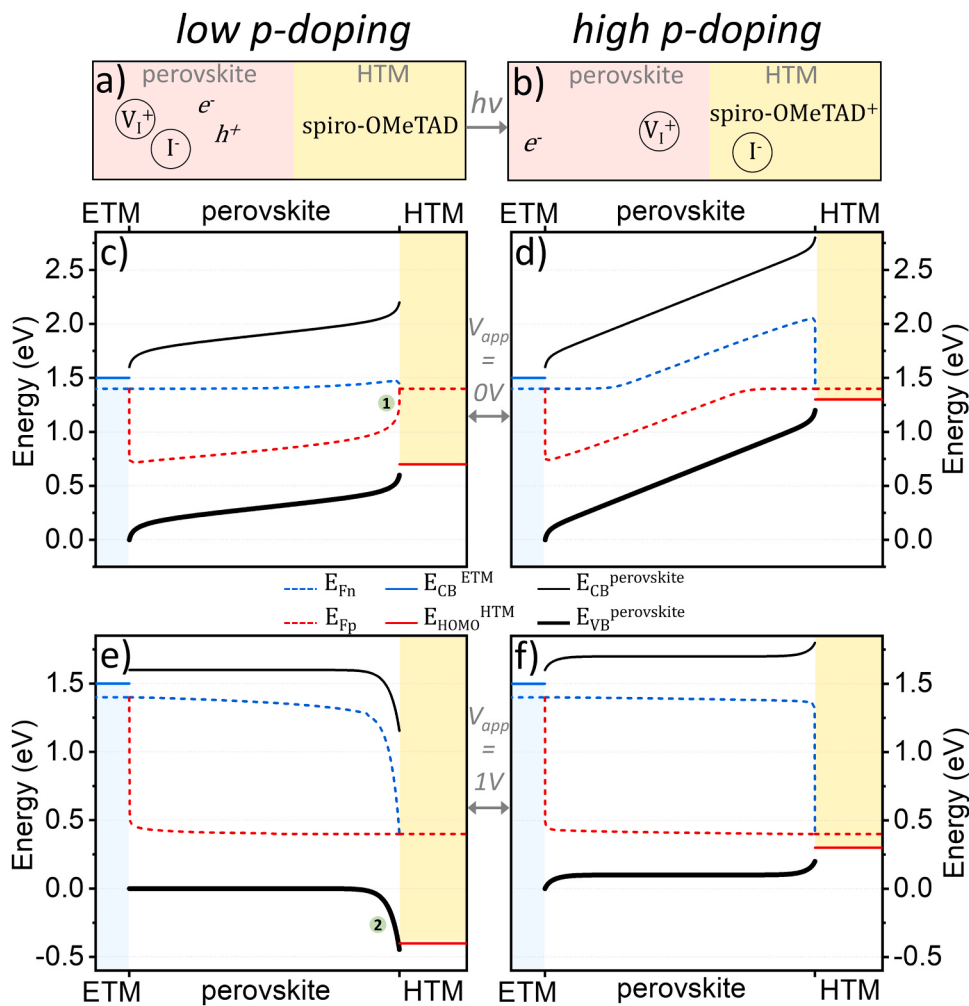


Fig. 7. a) J-V curves measured at different times of light soaking for a LC device. b) Photoluminescence mapping was measured simultaneously to the J-V curves shown in a), an average of the PL intensity within the device active area shown in the inset was taken and plotted as log (mean PL intensity) vs. V_{app} . Inset PL mapping is taken at 1.2 V at 6 h.



where iodide vacancies (V_I^+) and electrons (e^-) will remain in the perovskite and I^- in the HTM film as seen in Fig. 8b.

The presence of I^- in the HTM layer after overnight light soaking was studied by X-ray photoelectron spectroscopy (XPS) elemental depth profiles, however we could not find significant increase of this element compared to a non-illuminated sample (Fig. S6). The differences in the atomic percentages of the iodine is within the uncertainty. In the following, we provide more discussion to support the hypothesis of

Fig. 8. Diagram of the perovskite/HTM interface under illumination at a) the beginning of the light soaking time, where the HTM has low doping level and b) after long light soaking where the HTM is highly p-doped. Perovskite has photogenerated electrons (e^-) and holes (h^+) as well as mobile iodide ions (I^-) and iodide vacancies (V_I^+). Simplified representation of the energy level diagrams of the PSC for a low p-doped c), e) and highly p-doped HTM d), f), and at different applied voltages, $V_{app} = 0$ V c), d) and $V_{app} = 1$ V e), f). Number #1 in c) represents the large voltage drop at the perovskite interface and number #2 in e) shows the perovskite VB bending representing the hole injection barrier. E_{Fn} and E_{Fp} are the quasi Fermi level of electrons and holes, respectively.

iodide diffusion into the HTM. Assuming that the PCE improvement is directly related to the level of p-doping in HTM, we can infer that the processes described in Eq. 9(a-c) take place slowly, over 7 h of light soaking (see Fig. 1b). This oxidation of the HTM layer by the perovskite is slower than the reported photodoping mechanisms in air [48,52]. A possible cause is the slow ion diffusion speed in the HTM. Reactions in Eq. (10) and Eq. (11) will start at the interface of the HTM layer, slowly progressing towards the Au electrode. The larger radii of I^- will lead to

slower diffusion through the HTM compared to O_2 . The limited availability of mobile I^- or Br^- from the perovskite lattice compared to the large availability of O_2 from air would also result in the slow speed of this reaction. Moreover, we observed that when light soaking under short circuit condition, the PCE increase stops after the first 15 min (Fig. S1b). At short circuit condition, the larger availability of holes passing through the HTM would promote the reaction in Eq. (10), thus the doping speed may be expected to be higher. However, the large electric field at short circuit is reported to drive the anions to migrate and accumulate at the ETM interface [9]. The reduced availability of mobile I^- or Br^- at the perovskite/HTM interface is not sufficient to compensate the formed spiro-OMeTAD⁺ (see Eq. (11)), thus further oxidation through Eq. (10) will be restricted. Finally, in the absence of light, the perovskite ceases to photogenerate holes and spiro-OMeTAD⁺ slowly reverts to the neutral species, with I^- diffusing back to the perovskite layer.

We will now discuss the origin of the hole injection barrier at the perovskite/HTM interface. We have simulated the energy band diagrams at different conditions for devices employing the simulation tool reported by Bertoluzzi *et al.* [63]. Simulation details can be found in the Supporting Information. Based on the voltage- as well as time-dependent R_{inj} (Fig. 4 and Fig. 6) and PL (Fig. 7b) for low content of spiro-OMeTAD⁺, we can infer the existence of a barrier that impedes the extraction of holes from the perovskite. At early stages of the light soaking, the low *p*-doping of the HTM will result in a large energy separation between the work function (WF) and the highest occupied molecular orbital (HOMO) of the HTM. In an illuminated device, see Fig. 8c, e, the HTM WF will align with the device quasi-Fermi level of holes (E_{Fp}). Under short circuit conditions (Fig. 8c) the low HOMO level reduces the electric field in the perovskite, diminishing the driving force for charge extraction. At $V_{app} = 0$ V, the voltage drop causes an internal V_F close to open circuit conditions, thus resulting in high PL and low J_{sc} . This can be seen in Fig. 8c (#1) as the drop of E_{Fp} at the perovskite/HTM interface. The increased R_{inj} when increasing V_{app} (see Fig. 4a) can be explained in the band diagram as a progressive bending of the perovskite VB, see #2 in Fig. 8e for $V_{app} = 1$ V. With longer light soaking time, the increased *p*-doping will gradually reduce the separation between the HTM HOMO level and its E_{Fp} , or WF. This will increase the electric field improving the charge extraction at short circuit (Fig. 8d), as well as having favourable band alignment even at larger applied voltages, see Fig. 8f. The UPS spectra of two samples were measured, one that was always stored in the dark (dark) and the other was light soaked for 7 h (light) (Fig. S7a). The low energy cut-off reveals work functions of 4.15 and 4.20 eV while the valence band shows the onset of the HOMO levels at 1.38 and 1.27 eV, for the dark and light samples, respectively. The HOMO level shift suggests a *p*-doping of the HTM after light soaking. Band diagrams of the two samples have been produced based on the UPS analysis (see Fig. S7b).

Finally, we will discuss about the implications of the injection resistance in the impedance data analysis. When R_{inj} has large values, it shows a characteristic exponential increase with voltage, which is easy to interpret because it will be associated with extremely low device FF. However, when R_{inj} is small, it is only detectable at voltages around V_{oc} , with non-obvious influence on the PSC performance. This has important implications considering that many reports only analyse IS at one point around V_{oc} , and that the usual IS analysis attributes one arc feature to one physical process. Due to the proximity in the characteristic frequencies it is challenging to resolve the injection and recombination resistances by conventional IS data fitting. However, as suggested by Todinova *et al.* distribution of relaxation times (DRT) function modelling can be used instead [32].

3. Conclusion

We have adopted a series of characterisation methods including $J-V$, IS, Suns- V_{oc} and PL mapping to study the slow performance increase

during light soaking in PSCs with low content of spiro-OMeTAD⁺. We found that, even in the absence of LiTFSI and air exposure, the HTM can be photodoped under illumination increasing its conductivity. This suggests a gradual conversion of the neutral spiro-OMeTAD molecules to oxidised spiro-OMeTAD⁺. We propose a slow photodoping mechanism triggered by the transfer of photogenerated holes and limited by the slow migration of the halide anions from the perovskite into the HTM to neutralise the formed spiro-OMeTAD⁺. When the HTM has low content of spiro-OMeTAD⁺, a Schottky barrier exists at its interface with the perovskite impeding the charge extraction of photogenerated holes by the HTM. During light soaking, the Schottky barrier is reduced with increasing *p*-doping level in the HTM. Moreover, the inverse process takes place in the absence of light, during which the spiro-OMeTAD⁺ species are slowly reduced to neutral state. Therefore, the reversible transient process in light/dark treatment observed in this work can be simply explained by the photodoping of the HTM and the gradual removal of the hole extraction barrier.

From the IS analysis, we have unambiguously shown that the high frequency feature of IS has overlapping contributions from different physical processes. The Schottky barrier for hole injection acts as a voltage-dependent series resistance occurring at a similar frequency range as the high-frequency arc of the recombination process. As a result, the recombination resistance and geometric capacitance obtained from fitting the IS with the conventional equivalent circuit are greatly influenced by this injection barrier. We emphasise that the overlap of these two processes is not always as obvious as the extreme case shown in our work. Therefore, critical analysis of the IS data and support from complementary techniques are needed to avoid misinterpretations.

CRediT authorship contribution statement

B. Tan Conceived and designed the project, fabricated the devices and thin-film samples, wrote the manuscript. S.R. Raga Co-directed the project, analysed and interpreted the data, edited the manuscript. K.J. Rietwyk PL measurement, analysed and interpreted the data, edited the manuscript. J.F. Lu Analysed and interpreted data. S.O. Fürer Materials synthesis. J.C. Griffith Collected the UPS and XPS data. Y.-B. Cheng Analysed and interpreted data. U. Bach Analysed and interpreted data, directed the project.

Declaration of Competing Interest

The authors declare that they have no known competing financial interests or personal relationships that could have appeared to influence the work reported in this paper.

Acknowledgements

The authors are grateful for the financial support by the Australian Research Council (ARC) discovery project (DP160104575), the Australian Centre for Advanced Photovoltaics (ACAP), the Australian Renewable Energy Agency and the ARC Centre of Excellence in Exciton Science (ACEx: CE170100026). Sonia R. Raga acknowledges the support from "la Caixa" Foundation (ID 100010434), with fellowship code LCF/BQ/PI20/11760024 for funding part of this research. The authors would like to thank Dr. Luca Gael Bertoluzzi for the discussions and support for the band diagrams. The authors acknowledge use of the facilities within the Monash X-ray Platform.

Appendix A. Supporting information

Supplementary data associated with this article can be found in the online version at doi:10.1016/j.nanoen.2020.105658.

References

- [1] NREL, Best Research-Cell Efficiency Chart, 2020.
- [2] M.V. Khenkin, A.K. M, I. Visoly-Fisher, Y. Galagan, F. Di Giacomo, B.R. Patil, G. Sherafatipour, V. Turkovic, H.-G. Rubahn, M. Madsen, T. Merckx, G. Uytterhoeven, J.P.A. Bastos, T. Aernouts, F. Brunetti, M. Lira-Cantu, E.A. Katz, Reconsidering figures of merit for performance and stability of perovskite photovoltaics, *Energy Environ. Sci.* 11 (2018) 739–743.
- [3] M.V. Khenkin, E.A. Katz, A. Abate, G. Bardizza, J.J. Berry, C. Brabec, F. Brunetti, V. Bulović, Q. Burlingame, A. Di Carlo, R. Cheacharoen, Y.-B. Cheng, A. Colsmann, S. Cros, K. Domanski, M. Dusza, C.J. Fell, S.R. Forrest, Y. Galagan, D. Di Girolamo, M. Grätzel, A. Hagfeldt, E. von Hauff, H. Hoppe, J. Kettle, H. Köbler, M.S. Leite, S. Liu, Y.-L. Lou, J.M. Luther, C.-Q. Ma, M. Madsen, M. Manceau, M. Matheron, M. McGhee, R. Meitzner, M.K. Nazeeruddin, A.F. Nogueira, C. Odabaşı, A. Osherov, N.-G. Park, M.O. Reese, F. De Rossi, M. Saliba, U.S. Schubert, H. J. Snaith, S.D. Stranks, W. Tress, P.A. Troshin, V. Turkovic, S. Veenstra, I. Visoly-Fisher, A. Walsh, T. Watson, H. Xie, R. Yıldırım, S.M. Zakeeruddin, K. Zhu, M. Lira-Cantu, Consensus statement for stability assessment and reporting for perovskite photovoltaics based on ISOS procedures, *Nat. Energy* 5 (2020) 35–49.
- [4] K. Domanski, B. Roose, T. Matsui, M. Saliba, S.-H. Turren-Cruz, J.-P. Correa-Baena, C.R. Carmona, G. Richardson, J.M. Foster, F. De Angelis, J.M. Ball, A. Petrozza, N. Mine, M.K. Nazeeruddin, W. Tress, M. Grätzel, U. Steiner, A. Hagfeldt, A. Abate, Migration of cations induces reversible performance losses over day/night cycling in perovskite solar cells, *Energy Environ. Sci.* 10 (2017) 604–613.
- [5] M.V. Khenkin, A.K. M, I. Visoly-Fisher, S. Kolusheva, Y. Galagan, F. Di Giacomo, O. Vukovic, B.R. Patil, G. Sherafatipour, V. Turkovic, H.-G. Rubahn, M. Madsen, A. V. Mazanik, E.A. Katz, Dynamics of photoinduced degradation of perovskite photovoltaics: from reversible to irreversible processes, *ACS Appl. Energy Mater.* 1 (2018) 799–806.
- [6] S.-W. Lee, S. Kim, S. Bae, K. Cho, T. Chung, L.E. Mundt, S. Lee, S. Park, H. Park, M. C. Schubert, S.W. Glunz, Y. Ko, Y. Jun, Y. Kang, H.-S. Lee, D. Kim, UV degradation and recovery of perovskite solar cells, *Sci. Rep.* 6 (2016) 38150.
- [7] F. Liu, Q. Dong, M.K. Wong, A.B. Djurišić, A. Ng, Z. Ren, Q. Shen, C. Surya, W. K. Chan, J. Wang, A.M.C. Ng, C. Liao, H. Li, K. Shih, C. Wei, H. Su, J. Dai, Is excess PbI₂ beneficial for perovskite solar cell performance? *Adv. Energy Mater.* 6 (2016), 1502206.
- [8] F. Huang, L. Jiang, A.R. Pascoe, Y. Yan, U. Bach, L. Spiccia, Y.-B. Cheng, Fatigue behavior of planar CH₃NH₃PbI₃ perovskite solar cells revealed by light on/off diurnal cycling, *Nano Energy* 27 (2016) 509–514.
- [9] J. Carrillo, A. Guerrero, S. Rahimnejad, O. Almora, I. Zarazua, E. Mas-Marza, J. Bisquert, G. Garcia-Belmonte, Ionic reactivity at contacts and aging of methylammonium lead triiodide perovskite solar cells, *Adv. Energy Mater.* 6 (2016), 1502246.
- [10] C. Li, A. Guerrero, S. Huettner, J. Bisquert, Unravelling the role of vacancies in lead halide perovskite through electrical switching of photoluminescence, *Nat. Commun.* 9 (2018) 5113.
- [11] G. Liu, B. Yang, B. Liu, C. Zhang, S. Xiao, Y. Yuan, H. Xie, D. Niu, J. Yang, Y. Gao, C. Zhou, Irreversible light-soaking effect of perovskite solar cells caused by light-induced oxygen vacancies in titanium oxide, *Appl. Phys. Lett.* 111 (2017), 153501.
- [12] Y. Zhang, P. Wang, X. Yu, J. Xie, X. Sun, H. Wang, J. Huang, L. Xu, C. Cui, M. Lei, D. Yang, Enhanced performance and light soaking stability of planar perovskite solar cells using an amine-based fullerene interfacial modifier, *J. Mater. Chem. A* 4 (2016) 18509–18515.
- [13] A. Pockett, D. Raptis, S.M.P. Meroni, J. Baker, T. Watson, M. Carnie, Origin of exceptionally slow light soaking effect in mesoporous carbon perovskite solar cells with AVA additive, *J. Phys. Chem. C* 123 (2019) 11414–11421.
- [14] P. Wang, F. Cai, L. Yang, Y. Yan, J. Cai, H. Wang, R.S. Gurney, D. Liu, T. Wang, ACS Eliminating light-soaking instability in planar heterojunction perovskite solar cells by interfacial modifications, *ACS Appl. Energy Mater.* 10 (2018) 33144–33152.
- [15] Z. Song, J. Liu, G. Wang, W. Zuo, C. Liao, J. Mei, Understanding the photovoltaic performance of perovskite-spirobiifluorene solar cells, *ChemPhysChem* 18 (2017) 3030–3038.
- [16] E. Kasparavicius, A. Magomedov, T. Malinauskas, V. Getautis, Long-term stability of the oxidized hole-transporting materials used in perovskite solar cells, *Chem. Eur. J.* 24 (2018) 9910–9918.
- [17] F. Lamberti, T. Gatti, E. Cescon, R. Sorrentino, A. Rizzo, E. Menna, G. Meneghesso, M. Meneghetti, A. Petrozza, L. Franco, Evidence of spiro-OMeTAD de-doping by tert-butylpyridine additive in hole-transporting layers for perovskite solar cells, *Chem. Sust. Dev.* 5 (2019) 1806–1817.
- [18] Z. Hawash, L.K. Ono, S.R. Raga, M.V. Lee, Y. Qi, Air-exposure induced dopant redistribution and energy level shifts in spin-coated spiro-MeOTAD films, *Chem. Mater.* 27 (2015) 562–569.
- [19] Z. Li, C. Xiao, Y. Yang, S.P. Harvey, D.H. Kim, J.A. Christians, M. Yang, P. Schulz, S. U. Nanayakkara, C.-S. Jiang, J.M. Luther, J.J. Berry, M.C. Beard, M.M. Al-Jassim, K. Zhu, Extrinsic ion migration in perovskite solar cells, *Energy Environ. Sci.* 10 (2017) 1234–1242.
- [20] H. Wang, M. Xu, G. Liu, X. Li, P. Xiang, Z. Ku, Y. Rong, L. Liu, M. Hu, Y. Yang, H. Han, Effect of photo-doping on performance for solid-state dye-sensitized solar cell based on 2,2'7,7'-tetrakis-(N,N-di-p-methoxyphenyl-amine)-9,9'-spirobiifluorene and carbon counter electrode, *Electrochim. Acta* 99 (2013) 238–241.
- [21] X. Zhao, H.-S. Kim, J.-Y. Seo, N.-G. Park, Effect of selective contacts on the thermal stability of perovskite solar cells, *ACS Appl. Energy Mater.* 9 (2017) 7148–7153.
- [22] A.K. Jena, Y. Numata, M. Ikegami, T. Miyasaka, Role of spiro-OMeTAD in performance deterioration of perovskite solar cells at high temperature and reuse of the perovskite films to avoid Pb-waste, *J. Mater. Chem. A* 6 (2018) 2219–2230.
- [23] M. Saliba, M. Stolterfoht, C.M. Wolff, D. Neher, A. Abate, Measuring aging stability of perovskite solar cells, *Joule* 2 (2018) 1019–1024.
- [24] B. Tan, S.R. Raga, A.S.R. Chesman, S.O. Fürer, F. Zheng, D.P. McMeekin, L. Jiang, W. Mao, X. Lin, X. Wen, J. Lu, Y.-B. Cheng, U. Bach, LiTFSI-free spiro-OMeTAD-based perovskite solar cells with power conversion efficiencies exceeding 19%, *Adv. Energy Mater.* 9 (2019), 1901519.
- [25] W.H. Nguyen, C.D. Baillie, E.L. Unger, M.D. McGehee, Enhancing the hole-conductivity of spiro-OMeTAD without oxygen or lithium salts by using spiro (TFSI)₂ in perovskite and dye-sensitized solar cells, *J. Am. Chem. Soc.* 136 (2014) 10996–11001.
- [26] A. Sundqvist, O.J. Sandberg, M. Nyman, J.-H. Smått, R. Österbacka, Origin of the S-shaped JV curve and the light-soaking issue in inverted organic solar cells, *Adv. Energy Mater.* 6 (2016), 1502265.
- [27] F. Xu, J. Zhu, R. Cao, S. Ge, W. Wang, H. Xu, R. Xu, Y. Wu, M. Gao, Z. Ma, F. Hong, Z. Jiang, Elucidating the evolution of the current-voltage characteristics of planar organometal halide perovskite solar cells to an S-shape at low temperature, *Sol. Energy Mater. Sol. Cells* 157 (2016) 981–988.
- [28] Y. Liu, Q. Chen, H.-S. Duan, H. Zhou, Y. Yang, H. Chen, S. Luo, T.-B. Song, L. Dou, Z. Hong, Y. Yang, A dopant-free organic hole transport material for efficient planar heterojunction perovskite solar cells, *J. Mater. Chem. A* 3 (2015) 11940–11947.
- [29] H. Xi, S. Tang, X. Ma, J. Chang, D. Chen, Z. Lin, P. Zhong, H. Wang, C. Zhang, Performance enhancement of planar heterojunction perovskite solar cells through tuning the doping properties of hole-transporting materials, *ACS Omega* 2 (2017) 326–336.
- [30] M. Ulfa, T. Pauperté, T.-T. Bui, F. Goubard, Impact of organic hole transporting material and doping on the electrical response of perovskite solar cells, *J. Phys. Chem. C* 122 (2018) 11651–11658.
- [31] S.R. Raga, Y. Qi, The effect of impurities on the impedance spectroscopy response of CH₃NH₃PbI₃ perovskite solar cells, *J. Phys. Chem. C* 120 (2016) 28519–28526.
- [32] A. Todinova, L. Contreras-Bernal, M. Salado, S. Ahmad, N. Morillo, J. Idígoras, J. A. Anta, Towards a universal approach for the analysis of impedance spectra of perovskite solar cells: equivalent circuits and empirical analysis, *ChemElectroChem* 4 (2017) 2891–2901.
- [33] H. Zhang, L. Xue, J. Han, Y.Q. Fu, Y. Shen, Z. Zhang, Y. Li, M. Wang, New generation perovskite solar cells with solution-processed amino-substituted perylene diimide derivative as electron-transport layer, *J. Mater. Chem. A* 4 (2016) 8724–8733.
- [34] L. Contreras-Bernal, S. Ramos-Terrón, A. Riquelme, P.P. Boix, J. Idígoras, I. Mora-Seró, J.A. Anta, Impedance analysis of perovskite solar cells: a case study, *J. Mater. Chem. A* 7 (2019) 12191–12200.
- [35] A. Pockett, G.E. Eperon, N. Sakai, H.J. Snaith, L.M. Peter, P.J. Cameron, Microseconds, milliseconds and seconds: deconvoluting the dynamic behaviour of planar perovskite solar cells, *Phys. Chem. Chem. Phys.* 19 (2017) 5959–5970.
- [36] F. Ebadi, N. Taghavinia, R. Mohammadpour, A. Hagfeldt, W. Tress, Origin of apparent light-enhanced and negative capacitance in perovskite solar cells, *Nat. Commun.* 10 (2019) 1574.
- [37] I. Zarazua, G. Han, P.P. Boix, S. Mhaisalkar, F. Fabregat-Santiago, I. Mora-Seró, J. Bisquert, G. Garcia-Belmonte, Surface recombination and collection efficiency in perovskite solar cells from impedance analysis, *J. Phys. Chem. Lett.* 7 (2016) 5105–5113.
- [38] D. Moia, I. Gelmetti, P. Calado, W. Fisher, M. Stringer, O. Game, Y. Hu, P. Docampo, D. Lidzey, E. Palomares, J. Nelson, P.R.F. Barnes, Ionic-to-electronic current amplification in hybrid perovskite solar cells: ionically gated transistor-interface circuit model explains hysteresis and impedance of mixed conducting devices, *Energy Environ. Sci.* 12 (2019) 1296–1308.
- [39] Z. Zolfaghari, E. Hassanabadi, D. Pitarch-Tena, S.J. Yoon, Z. Sharatinia, J. van de Lagemaat, J.M. Luther, I. Mora-Seró, Operation mechanism of perovskite quantum dot solar cells probed by impedance spectroscopy, *ACS Energy Lett.* 4 (2019) 251–258.
- [40] D.A. Jacobs, H. Shen, F. Pfeffer, J. Peng, T.P. White, F.J. Beck, K.R. Catchpole, The two faces of capacitance: new interpretations for electrical impedance measurements of perovskite solar cells and their relation to hysteresis, *J. Appl. Phys.* 124 (2018), 225702.
- [41] N. Pellet, Ph.D. Thesis, Investigations on hybrid organic-inorganic perovskites for high performance solar cells, EPFL, 2017.
- [42] E.J. Juarez-Perez, M. Wujpler, F. Fabregat-Santiago, K. Lakus-Wolny, E. Mankel, T. Mayer, W. Jaegermann, I. Mora-Seró, Role of the selective contacts in the performance of lead halide perovskite solar cells, *J. Phys. Chem. Lett.* 5 (2014) 680–685.
- [43] A. Guerrero, G. Garcia-Belmonte, I. Mora-Seró, J. Bisquert, Y.S. Kang, T. J. Jacobsson, J.-P. Correa-Baena, A. Hagfeldt, Properties of contact and bulk impedances in hybrid lead halide perovskite solar cells including inductive loop elements, *J. Phys. Chem. C* 120 (2016) 8023–8032.
- [44] M. Anaya, W. Zhang, B.C. Hames, Y. Li, F. Fabregat-Santiago, M.E. Calvo, H. J. Snaith, H. Míguez, I. Mora-Seró, Electron injection and scaffold effects in perovskite solar cells, *J. Mater. Chem. C* 5 (2017) 634–644.
- [45] M. Bag, L.A. Renna, R.Y. Adhikari, S. Karak, F. Liu, P.M. Lahti, T.P. Russell, M. T. Tuominen, D. Venkataraman, Kinetics of ion transport in perovskite active layers and its implications for active layer stability, *J. Am. Chem. Soc.* 137 (2015) 13130–13137.
- [46] M. Ulfa, P. Wang, J. Zhang, J. Liu, W.D. de Marcillac, L. Coolen, S. Peralta, T. Pauperté, Charge injection and electrical response in low-temperature SnO₂-based efficient perovskite solar cells, *ACS Appl. Energy Mater.* 10 (2018) 35118–35128.

- [47] S.-M. Yoo, S.J. Yoon, J.A. Anta, H.J. Lee, P.P. Boix, I. Mora-Seró, An equivalent circuit for perovskite solar cell bridging sensitized to thin film architectures, Joule 10 (2019) 2535–2549.
- [48] A. Abate, T. Leijtens, S. Pathak, J. Teuscher, R. Avolio, M.E. Errico, J. Kirkpatrick, J. M. Ball, P. Docampo, I. McPherson, H.J. Snaith, Lithium salts as “redox active” p-type dopants for organic semiconductors and their impact in solid-state dye-sensitized solar cells, Phys. Chem. Chem. Phys. 15 (2013) 2572–2579.
- [49] T.M. Koh, S. Dharani, H. Li, R.R. Prabhakar, N. Mathews, A.C. Grimsdale, S. G. Mhaisalkar, Cobalt dopant with deep redox potential for organometal halide hybrid solar cells, ChemSusChem 7 (2014) 1909–1914.
- [50] J. Burschka, A. Dualeh, F. Kessler, E. Baranoff, N.-L. Cevey-Ha, C. Yi, M. K. Nazeeruddin, M. Grätzel, Tris(2-(1H-pyrazol-1-yl)pyridine)cobalt(III) as p-type dopant for organic semiconductors and its application in highly efficient solid-state dye-sensitized solar cells, J. Am. Chem. Soc. 133 (2011) 18042–18045.
- [51] S. Wang, W. Yuan, Y.S. Meng, Spectrum-dependent spiro-OMeTAD oxidation mechanism in perovskite solar cells, ACS Appl. Energy Mater. 7 (2015) 24791–24798.
- [52] R.S. Sanchez, E. Mas-Marza, Light-induced effects on spiro-OMeTAD films and hybrid lead halide perovskite solar cells, Sol. Energy Mater. Sol. Cells 158 (2016) 189–194.
- [53] O. Almora, K.T. Cho, S. Aghazada, I. Zimmermann, G.J. Matt, C.J. Brabec, M. K. Nazeeruddin, G. Garcia-Belmonte, Discerning recombination mechanisms and ideality factors through impedance analysis of high-efficiency perovskite solar cells, Nano Energy 48 (2018) 63–72.
- [54] W. Tress, M. Yavari, K. Domanski, P. Yadav, B. Niesen, J.P. Correa Baena, A. Hagfeldt, M. Graetzel, Interpretation and evolution of open-circuit voltage, recombination, ideality factor and subgap defect states during reversible light-soaking and irreversible degradation of perovskite solar cells, Energy Environ. Sci. 11 (2018) 151–165.
- [55] J.-P. Correa-Baena, S.-H. Turren-Cruz, W. Tress, A. Hagfeldt, C. Aranda, L. Shooshtari, J. Bisquert, A. Guerrero, Changes from bulk to surface recombination mechanisms between pristine and cycled perovskite solar cells, ACS Energy Lett. 2 (2017) 681–688.
- [56] P. Calado, D. Burkitt, J. Yao, J. Troughton, T.M. Watson, M.J. Carnie, A.M. Telford, B.C. O'Regan, J. Nelson, P.R.F. Barnes, Identifying dominant recombination mechanisms in perovskite solar cells by measuring the transient ideality factor, Phys. Rev. Appl. 11 (2019), 044005.
- [57] K. Tvingstedt, C. Deibel, Temperature dependence of ideality factors in organic solar cells and the relation to radiative efficiency, Adv. Energy Mater. 6 (2016), 1502230.
- [58] S. Agarwal, M. Seetharaman, N.K. Kumawat, A.S. Subbiah, S.K. Sarkar, D. Kabra, M.A.G. Namboothiry, P.R. Nair, On the uniqueness of ideality factor and voltage exponent of perovskite-based solar cells, J. Phys. Chem. Lett. 5 (2014) 4115–4121.
- [59] F. De Castro, A. Laudani, F. Riganti Fulginei, A. Salvini, An in-depth analysis of the modelling of organic solar cells using multiple-diode circuits, Sol. Energy 135 (2016) 590–597.
- [60] B. Romero, G. Del Pozo, E. Destouesse, S. Chambon, B. Arredondo, Circuital modelling of S-shape removal in the current–voltage characteristic of TiO_x inverted organic solar cells through white-light soaking, Org. Electron. 15 (2014) 3546–3551.
- [61] F.J. García-Sánchez, D. Lugo-Muñoz, J. Muci, A. Ortiz-Conde, Lumped parameter modeling of organic solar Cells' S-shaped I-V characteristics, IEEE J. Photovolt. 3 (2013) 330–335.
- [62] F. Ad Castro, J. Heier, F. Nüesch, R. Hany, Origin of the kink in current-density versus voltage curves and efficiency enhancement of polymer-C60 heterojunction solar cells, IEEE J. Sel. Top. Quantum Electron. 16 (2010) 1690–1699.
- [63] L. Bertoluzzi, C.C. Boyd, N. Rolston, J. Xu, R. Prasanna, B.C. O'Regan, M. D. McGehee, Mobile ion concentration measurement and open-access band diagram simulation platform for halide perovskite solar cells, Joule 4 (2020) 109–127.